From hexagonal to rocksalt structure: A computational study of gallium selenide under hydrostatic pressure

Vo Khuong Dien,[1] Nguyen Thanh Tien,[2] Nguyen Duy Khanh,[3,4,*] Nguyen Thi Ngoc Han,[5] and Ming-Fa Lin[6,7]

[1]*Department of Electrophysics, National Yang Ming Chiao Tung University, Hsinchu 300, Taiwan*
[2]*College of Natural Sciences, Can Tho University, 3-2 Road, Can Tho City 94000, Vietnam*
[3]*Laboratory for Computational Physics, Institute for Computational Science and Artificial Intelligence, Van Lang University, Ho Chi Minh City 70000, Vietnam*
[4]*Faculty of Mechanical - Electrical and Computer Engineering, School of Technology, Van Lang University, Ho Chi Minh City 70000, Vietnam*
[5]*Fschool Can Tho, FPT University, 600 Nguyen Van Cu Street, Can Tho City 900000, Vietnam*
[6]*Department of Physics, National Cheng Kung University, 701 Tainan, Taiwan*
[7]*Hierarchical Green-Energy Material (Hi-GEM) Research Center, National Cheng Kung University, 701 Tainan, Taiwan*

(Received 6 April 2023; revised 25 September 2023; accepted 1 November 2023; published 27 November 2023; corrected 15 April 2024)

The understanding of pressure-dependent fundamental properties of materials is very essential, not only for basic scientific knowledge but also for advanced technological applications. Experimental observations have fully revealed the hexagonal-to-rocksalt phase transition in the GaSe system under high pressure. In this article we systematically investigate the pressure-induced structural phase transition and related phonon, electronic, and optical properties of hexagonal ε-GaSe through a complete first-principles theoretical framework developed by the density-functional-theory calculations. The study focuses on geometric optimization, electronic band structures, electron localization functions, phonon spectra, dielectric properties, and optical spectra of the GaSe system under hydrostatic pressure. This work also includes an analysis of the phase transformation mechanism using the solid-state nudged elastic band method. Our research sheds light on the physics of structural phase transitions in layered materials and offers potential for the development of pressure-manipulated electronics and optoelectronics.

DOI: 10.1103/PhysRevB.108.205150

I. INTRODUCTION

Group-III monochalcogenides (MX, M = Ga, In; X = S, Se, Te) are currently a topic of interest [1–3] due to their unique properties and their potential applications in various fields such as high-harmonic generation [4,5], optoelectronics [6–8], photovoltaics [9,10], and photocatalytic water splitting [11,12]. Among MX compounds, gallium selenide (GaSe) holds a central position due to its particularly intriguing properties. The adjacent layers of GaSe are weakly held together through van der Waals (VdW) interactions, while the bonding within each layer between the post-transition-metal and chalcogenide atoms is primarily governed by covalent couplings. Interlayer interactions in GaSe have been extensively studied in previous research [13–15], revealing that they are relatively weak, with the cleavage energy of bulk GaSe being much smaller than that of graphite and MoS_2, making it easy to isolate monolayers [16–18].

According to earlier theoretical and experimental investigations, bulk GaSe is a material with a wide electronic band gap. It undergoes a direct-to-indirect band-gap transition when the number of layers decreases below a critical value [19,20]. This transition is in contrast to the behavior observed in transition-metal dichalcogenides [21]. In addition to its electronic properties, layered GaSe also exhibits unique and extraordinary excitonic effects. GaSe demonstrated a strong photoresponse in recent experiments [22]. Theoretical predictions by Antonius and co-workers indicated that the absorbance spectra of GaSe exhibit featured exciton peaks with distinct polarization selectivity. These interesting phenomena arise from the symmetry of the bands in the presence of mirror symmetry [23]. Recently, theoretical calculations by Dien *et al.* also pointed out that the electronic properties and excitonic effects of single-layer GaSe are sensitive to mechanical strains [24].

Materials at high pressure occur at the center of the planets or stars and can also be achieved in the laboratory via the diamond anvil cell (DAC) device [25]. The relative stability phases and possible transformations between them under extremely high pressure have a long-standing interest [25–29]. The knowledge about pressure being dependent on electronic and optical properties is essential not only for basic sciences but also for high-tech applications [30–33]. Up to now, several groups have conducted research on the high-pressure phase transformation of group-MX-based materials utilizing *ab initio* investigations [34] and high-pressure measurements [35]. In the case of GaSe, the hexagonal-to-rocksalt phase transition occurs in a pressure range of 21–25 GPa, as confirmed by x-ray diffraction in a DAC device [35–38]. The transition value is approximately 20 GPa when considering a freestanding

*Corresponding author: khanh.nguyenduy@vlu.edu.vn

screw-dislocation-driven (SDD) GaSe thin film [37]. On the other hand, first-principles calculations by Ghalouci *et al.* [34] found that the hexagonal-to-rocksalt phase transition occurs at 17.74 GPa. Additionally, the electronic and optical properties of GaSe are predicted to be highly sensitive to external hydrostatic pressure [39,40], making GaSe suitable for the development of broadband light sources and high-performance pressure sensors.

Despite significant interest in recent years, there is a lack of theoretical predictions concerning the pressure-dependent phase transition of GaSe and its associated geometric, atomic vibration, electronic, and optical properties. Furthermore, critical mechanisms and theoretical explanations of the properties of GaSe are still absent. The phase transformation of GaSe remains incompletely understood. Therefore it is crucial to conduct a theoretical investigation to gain insights into the systematic behavior of the phase transition in GaSe and to explore its potential applications.

In this work the phase transition and related electronic and optical properties of hexagonal ε-GaSe are discussed in detail. The strategy relies on first-principles calculations with detailed analyses. Orbital hybridizations in the chemical bonding and the phase transitions are clarified based on the geometric optimization, accurate electronic band structures, and the electron localization functions (ELFs). The optical properties are analyzed based on the dielectric functions, absorbance and reflectance spectra, and electron energy-loss functions. In addition, we thoroughly investigate the evolution of excitonic effects under the influence of hydrostatic pressure by solving the Bethe-Salpeter equation (BSE). The phase transformation mechanism is analyzed using the solid-state nudged elastic band (SS-NEB) method.

II. COMPUTATIONAL DETAILS

To optimize the geometric structure and calculate the electronic and optical properties of bulk GaSe, we employed the Vienna Ab-initio Simulation Package (VASP) with the Perdew-Burke-Ernzerhof (PBE) generalized gradient approximation for the exchange-correlation function. We used projector-augmented wave (PAW) pseudopotentials with a cutoff energy of 500 eV to describe the electron-ion interactions. The atomic configuration of $3d^{10}4s^24p^1$ and $4s^24p^4$ for Ga and Se atoms, respectively, were treated as valence. Additionally, we adopted the VdW-DFT-D2 method of Grimme *et al.* [41], which has demonstrated reasonable accuracy for layered systems, for our calculations. Geometric optimization was performed using a Monkhorst-Pack sampling technique with a special k-point mesh of $25 \times 25 \times 4$ and $15 \times 15 \times 15$ for hexagonal and rocksalt phases, respectively. During optimization, all atoms are fully relax until the Hellmann-Feynman force acting on each atom was less than 0.01 eV/Å, and we set the convergence condition to 10^{-8} eV between two consecutive simulation steps.

The phonon dispersions and polarizations of GaSe were obtained using harmonic approximations. To obtain reliable force constants for hexagonal and rocksalt GaSe, supercells of $4 \times 4 \times 2$ and $3 \times 3 \times 3$ were generated, respectively, using the PHONOPY codes [42]. Additionally, Born effective charges (Z^*) and dielectric constants (ε) were calculated using density-functional perturbation theory (DFPT) as a correction to account for long-range electrostatic interactions in the dynamical matrix (Fig. S4 in Supplemental Material [43]).

The quasiparticle energy spectrum was obtained using the GW approximation (G0W0) [44] on the exchange-correlation self-energy. The plane-wave expansion was truncated at a cutoff energy of 500 eV, and response functions were truncated at 150 eV. The Brillouin zone was integrated with a $20 \times 20 \times 3$ k-point mesh and a $12 \times 12 \times 12$ k-point mesh in the Γ sampling technique for the hexagonal and the rocksalt phases, respectively. The quasi band structure was plotted using the Wannier interpolation procedure in the WANNIER90 code [45].

To incorporate excitonic effects in optical properties, we solved the Bethe-Salpeter equation (BSE) [46] of the interacting two-particle Green's function. In this calculation, the Tamm-Dancoff approximation (TDA) [47], which has given accurate results for the optical absorption spectra of other metallic systems such as metallic carbon nanotubes [48], doped graphene [49], and copper (Fig. S10 in Supplemental Material [43]), was used. A Lorentzian function with a broadening of up to 50 meV was used to replace the delta function. The excitonic effects were described using the six lowest conduction bands (CBs) and the eight highest valence bands (VBs) in the Bethe-Salpeter kernel.

III. RESULTS AND DISCUSSION

A. Geometric structure

Based on the stacking configuration, bulk GaSe exhibits four distinct phases at ambient conditions ($P = 0$ GPa): $\varepsilon - (2H'/D3h)$, $\beta - (2H/D6h)$, $\gamma - (3R/C3v)$, and $\delta - (4H/C6v)$ [15], as illustrated in Fig. S1 [43]. Previous experimental growths and first-principles calculations have demonstrated that ε-GaSe and γ-GaSe are commonly observed phases in epitaxial films and their bulk counterpart. The primary focus of this study is to investigate the structural phase transition of hexagonal ε-GaSe under hydrostatic pressure. The unit cell of ε-GaSe consists of two GaSe layers, each displaying a binary, arseniclike structure [50]. The Ga and Se atoms within each layer form a trigonal prismatic arrangement, with strong covalent bonds between Ga and Ga, as well as Ga and Se atoms [Fig. 1(c)]. Since the Van der Waals (VdW) interactions between the individual atomic sheets are relatively weak but still exert some influence on the optimal geometric structure, we evaluated the optimized parameters of GaSe using various exchange-correlation functionals. The optimized lattice constants for ε-GaSe, calculated with VdW-DFT-D2 correction, were found to be $a = 3.745$ Å and $c = 15.921$ Å. These values are consistent with previous experimental [51–53] and theoretical studies [34,54] mentioned in Table I and Fig. S2 [43]. Consequently, we selected the VdW-DFT-D2 functional for the current investigation. The high-pressure phase [rocksalt phase in Fig. 1(b)] exhibits a face-centered cubic structure with three orthogonal axes, where Ga and Se atoms form an octahedral arrangement [see Fig. 1(c)].

Figure 1(d) illustrates cohesive energy and enthalpy diagrams for both the hexagonal and rocksalt phases of GaSe. Under ambient pressure conditions, the rocksalt phase is less stable than the hexagonal phase, as indicated by its lower cohesive and enthalpy energies. Our findings suggest a tran-

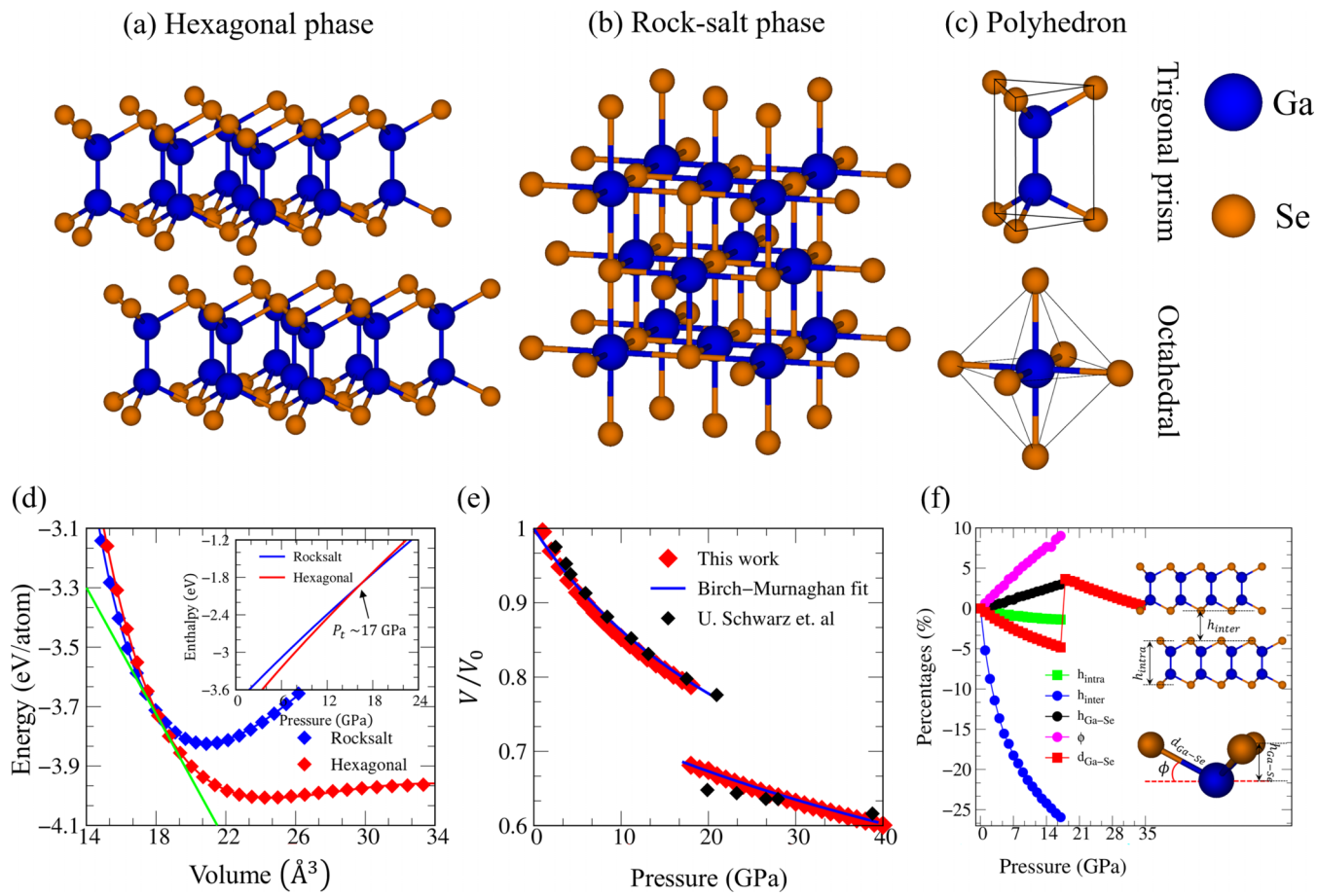

FIG. 1. The geometric structure of GaSe with (a) hexagonal ε phase ($P = 0$ GPa), (b) rocksalt phase ($P = 18$ GPa), and (c) the Ga-Se polyhedron. (d) Cohesive energy as a function of volume for the hexagonal and the rocksalt phases of GaSe. The inset indicates the corresponding pressure-dependent enthalpy. The equilibrium transition pressure P_t is estimated at ~17 GPa. (e) The evolution of the lattice volume under hydrostatic pressure. The previous experiment measurement [59] is also plotted for comparison. (f) The change in geometric parameters with increasing pressure, and illustrations of geometric parameters for hexagonal GaSe.

sition pressure (P_t) of approximately 17 GPa, which is consistent with previous theoretical studies [34]. Regarding the experimental aspect, Schwarz *et al.* have revealed a phase transition of ε-GaSe occurring around 21 GPa [36]. Diep *et al.* have presented a pressure-driven hexagonal-to-rocksalt transition in subfree SDD-GaSe films at approximately 20 GPa, whereas for bulk samples, the transition occurred within the range of 22–25 GPa [37]. The underestimation of the transition pressure in our study, compared to experimental observations, can be attributed to certain simplifications and approximations in theoretical calculation. Additionally, it is important to acknowledge that our computations were performed at 0 K and did not account for the influence of phonon.

The red-square dots in Fig. 1(e) show the change in volume of the unit cell upon the applied hydrostatic pressure, while the blue-solid curve shows the fitting results using the third-order Birch-Murnaghan equation of state (BM EoS) [29,60]:

$$P = \frac{3}{2}B_0\left[\left(\frac{V_0}{V}\right)^{\frac{7}{3}} - \left(\frac{V_0}{V}\right)^{\frac{5}{3}}\right] \times \left\{1 + \frac{3}{4}(B_0' - 4)\left[\left(\frac{V_0}{V}\right)^{\frac{2}{3}} - 1\right]\right\}, \quad (1)$$

where B_0, B_0', V_0, and V are, in turn, the ambient pressure bulk modulus, its pressure derivative, the fitting parameter that corresponds to the extrapolated unit-cell volume of the phase being considered, and pressure-dependent unit-cell volume. The calculated coefficients of the BM EoS for the hexagonal structure are $B_0 = 54.54$ GPa and $B_0' = 2.84$, and for the rocksalt phase are $B_0 = 153$ GPa and $B_0' = 3.1$. Generally, the compressing volume nearly monotonously decreases with pressure increase and gets a dramatic change at the critical pressure ~17 GPa. Quantitatively, the volume variation $\Delta V = |V - V_0|/V_0$ is about 10% and is compatible with the more than 8% observed in previous work [36]. The pressure-volume diagram is in good agreement with experimental measurements [36] [the black-square dot in Fig. 1(e)].

In the stability field of the ε-GaSe, the presence of intralayer height (h_{inter}), interlayer distance (h_{intra}), the Ga-Se height difference ($h_{\text{Ga-Se}}$), the Ga-Se bond length ($d_{\text{Ga-Se}}$), and the angle (ϕ) between the Ga-Se bond and the Se atom sheet can provide insights into the deformations of GaSe under hydrostatic pressures [Fig. 1(f)]. At a pressure below 17 GPa, the interlayer distance gradually decreased up to 25% at $P \sim 17$ GPa, mainly due to the weak VdW force, causing a gradual shrinkage of the vertical lattice constant c of GaSe

TABLE I. The calculated and experimental lattice parameters, intralayer height h_{intra}, interlayer distance h_{inter}, the Ga-Ga bond length $d_{Ga\text{-}Se}$, the Ga-Se bond length $d_{Ga\text{-}Se}$ (in Å), and unit-cell volume V_0 (in Å^3) of ε-GaSe under ambient conditions were examined. To compare the results, various exchange-correlation functionals were employed: local-density approximation (LDA), Perdew-Burke-Ernzerhof (PBE) generalized gradient approximation, VdW-DFT-D2 method developed by Grimme, DFT-D3 method of Grimme with zero-damping function, DFT-D3 method with Becke-Johnson damping function.

	a	c	V_0	h_{inter}	h_{intra}	$h_{Ga\text{-}Se}$	$d_{Ga\text{-}Ga}$
LDA	3.718[a]	15.64[a]	187.392[a]	3.090[a]	4.732[a]	2.441[a]	2.406[a]
	3.719[b]	15.611[b]	186.9[b]	3.071[b]	4.734[b]	2.442[b]	2.405[b]
PBE	3.818[a]	17.673[a]	223.160[a]	4.021[a]	4.816[a]	2.497[a]	2.470[a]
	3.823[b]	17.848[b]	225.9[b]	4.106[b]	4.819[b]	2.500[b]	2.470[b]
PBE-D2	3.745[a]	15.921[a]	193.476[a]	3.154[a]	4.806[a]	2.467[a]	2.429[a]
	3.749[b]	15.931[b]	193.9[b]	3.154[b]	4.812[b]	2.470[b]	2.430[b]
PBE-D3 zero-damping	3.801[a]	16.040[a]	200.705[a]	3.246[a]	4.773[a]	2.483[a]	2.446[a]
PBE-D3 Becke-Johnson	3.774[a]	15.876[a]	197.256[a]	3.173[a]	4.801[a]	2.445[a]	2.477[a]
X ray	3.749[c]	15.907[c]	193.6[c]	–	–	–	–
	3.755[d]	15.946[d]	194.7[d]	–	–	–	–
	3.759[e]	15.968[e]	195.4[e]	–	–	–	–
	3.755[f]	15.98[f]	195.13[f]	–	–	–	–

[a]This work.
[b]Reference [55].
[c]Reference [56].
[d]Reference [57].
[e]Reference [36].
[f]Reference [58].

[37]. However, the intralayer h_{intra} remained almost constant. The GaSe chemical bond length $d_{Ga\text{-}Se}$, on the other hand, significantly reduced and changed drastically at ∼17 GPa, indicating the phase transition. Despite a 5% reduction in $d_{Ga\text{-}Se}$, $h_{Ga\text{-}Se}$ increased mildly by about 3% due to an increase in the angle ϕ from 27.9° to 30.4°, leading to reduction of the in-plane atomic interactions of Ga and Se atoms. The observed chemical modifications are expected to dramatically impact the electronic and optical properties of GaSe through alterations in overlap and separation of orbitals.

B. Atomic vibrations and phonon properties

The phonon band structures of the GaSe under six different pressures are presented in Fig. 2, in which two in-plane acoustic modes (LA and ZA) of the hexagonal ε-GaSe shown in Fig. 2(a) exhibit a linear dispersion with higher frequencies compared to the out-of-plane acoustic mode (ZA) at the long-wavelength limit. The ZA mode, similar to layered materials such as graphite [61] and MoS_2 [62], follows a quadratic dependence and plays a significant role in the material's thermal properties at low temperatures. The VdW interactions between the GaSe layers lead to low-frequency optical modes at 20.05 cm^{-1} and 36.38 cm^{-1}, corresponding to rigid-layer shear (LO′ and TO′) and vertical (ZO′) motions, respectively. These soft vibration modes dominate the low-temperature heat capacity (Figs. S6(a) and S6(b) [43]). Furthermore, there is a large phonon band gap between the low-frequency optical phonon branches and other optical modes. The origin of this phonon band gap can be attributed to two fundamental factors: the variance in atomic mass between Ga and Se, as well as the distinction in the strength of atomic interactions in Ga-Se and Ga-Ga chemical bonds. The first factor can be readily elucidated through the application of the diatomic linear chain model [63], which suggests that the phonon band gap between the acoustic and optical modes at the zone boundary is directly proportional to the mass difference between the involved elements. On the other hand, the second factor is associated with bond strength, which is inherently linked to phonon frequencies. For instance, the Ga-Ga and Ga-Se bonds exhibit distinct atomic distances, resulting in variations in the strength of atomic interactions. These variations significantly impact the distribution of phonon frequencies, ultimately influencing the formation of the band gap [64].

As the compression pressure increases [as shown in Figs. 2(b) and 2(c)], the bandwidth of the GaSe phonon band structure gradually expands toward higher frequencies. This expansion occurs due to the reduction in the vertical VdW gap and the significant shortening of intralayer bond lengths. Notably, there is enhanced dispersion in phonon branches near the Γ point, indicating higher group velocities. On the other hand, the LA and TA phonon branches become progressively softer around high-symmetry points such as M, K, L, and H. These observed phenomena directly impact phonon accumulation (Fig. S5 [43]) and significantly alter the phonon specific heat capacity (Fig. S6(d) [43]) of GaSe. Figures 2(d)–2(f) depict the phonon band structure of GaSe in its high-pressure rocksalt phase, which exhibits notable differences compared to the previous discussion. In this phase, the significant phonon band gap observed in the hexagonal phase is absent and the phonon branches with greater dispersion can be detected. Importantly, the absence of imaginary frequencies in the phonon band structure of any sample indicates the dynamic stability of GaSe under various pressures.

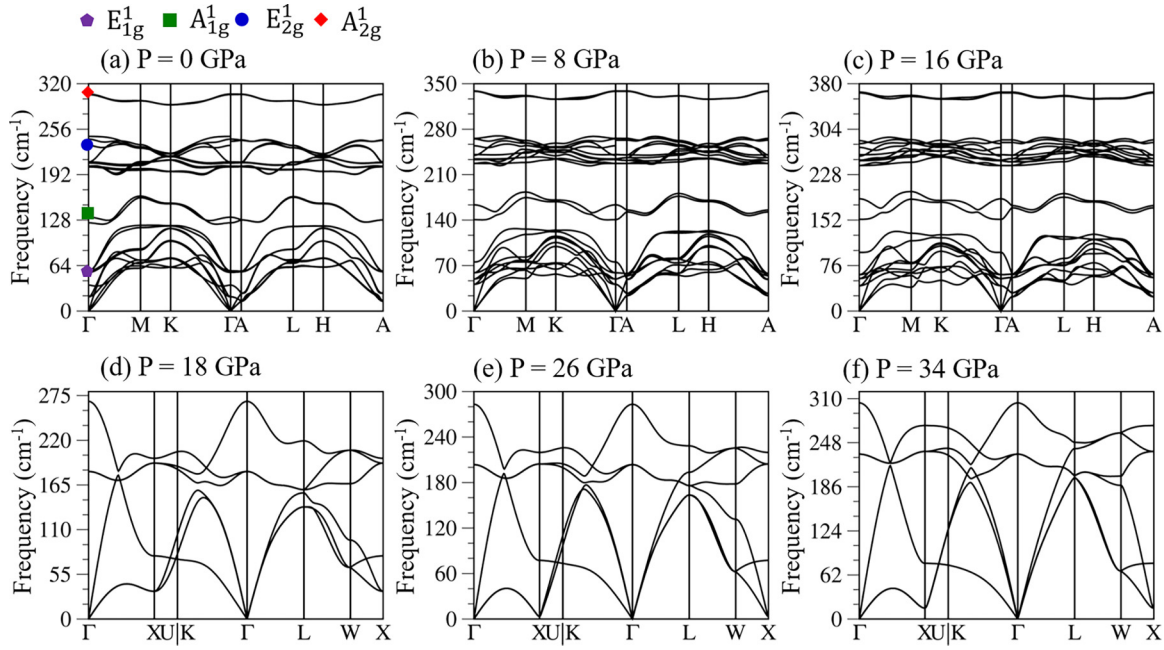

FIG. 2. Calculated phonon dispersions for GaSe under six presentative pressures: hexagonal GaSe at (a) 0 GPa, (b) 8 GPa, (c) 16 GPa, and rocksalt GaSe at (d) 18 GPa, (e) 26 GPa, and (f) 34 GPa. The Raman-active modes of hexagonal GaSe are marked by the color symbols.

To gain deeper insight into the evolution of phonon vibrations under varying pressure conditions, we conducted a comprehensive analysis of the active Raman modes as a function of pressure, along with their corresponding vibration modes, as illustrated in Fig. 3. Notably, the spectral data only extend up to 17 GPa, as the rocksalt phase of GaSe is Raman inactive due to its inversion symmetry structure [59,65]. At the ambient pressure, the hexagonal phase of ε-GaSe exhibits four distinct Raman modes: E^1_{1g}, A^1_{1g}, E^2_{2g}, and A^2_{1g} located at 56.52 cm^{-1}, 131.79 cm^{-1}, 232.74 cm^{-1}, and 304.91 cm^{-1}, respectively. For comparison, the experimental values are also listed in Table II. The overall agreement between theoretical values and experimental measurements is quite good. As pressure increases, all of the active Raman modes increase linearly in frequency, reflecting a broadening of the phonon band structure and accompanying lattice shrinkage. The changing rates of these modes are 0.28 cm^{-1} GPa, 4.01 cm^{-1} GPa, 2.73 cm^{-1} GPa, and A^2_{1g} = 4.26 cm^{-1} GPa, respectively, for E^1_{1g}, A^1_{1g}, E^2_{2g}, and A^2_{1g} Raman-active modes. It is worth noting that the out-of-plane vibration modes, specifically A^1_{1g} and A^2_{1g}, experience faster change than the others, such as E^1_{1g}. This discrepancy is attributed to the greater sensitivity of the c-axis compression, primarily influenced by weak VdW forces. As the pressure increases, the distance between layers decreases and the interlayer interaction is strongly enhanced, leading to a rapid increase in the frequency of A^1_{1g} and A^2_{1g} modes. In

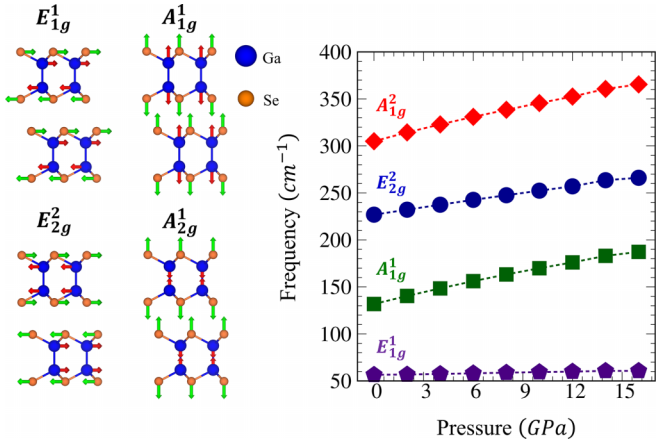

FIG. 3. The pressure-dependent Raman-active modes of hexagonal ε-GaSe and visualized configuration of the corresponding Raman-active vibration modes.

TABLE II. Vibration direction, calculated frequency, and the changing rate ($d\omega/dP$) of the relevant Raman-active modes. The measurement data of the prior works are also listed for comparison.

Mode parameter	Direction	Frequency (cm^{-1})	$d\omega/dP$ (cm^{-1}/GPa)
E^1_{1g}	In plane	56.55[a]	0.28[a]
		58.8[b]	0.26[b]
		60.1[c]	–
A^1_{1g}	Out of plane	131.85[a]	4.01[a]
		133.1[b]	4.96[b]
		134.6[c]	–
E^2_{2g}	In plane	232.79[a]	2.73[a]
		251.4[b]	2.35[b]
A^2_{1g}	Out of plane	305.0[a]	4.26[a]
		308.1[b]	3.85[b]
		307.8[c]	–

[a]This work.
[b]Measurement data from Ref. [37].
[c]Measurement data from Ref. [13].

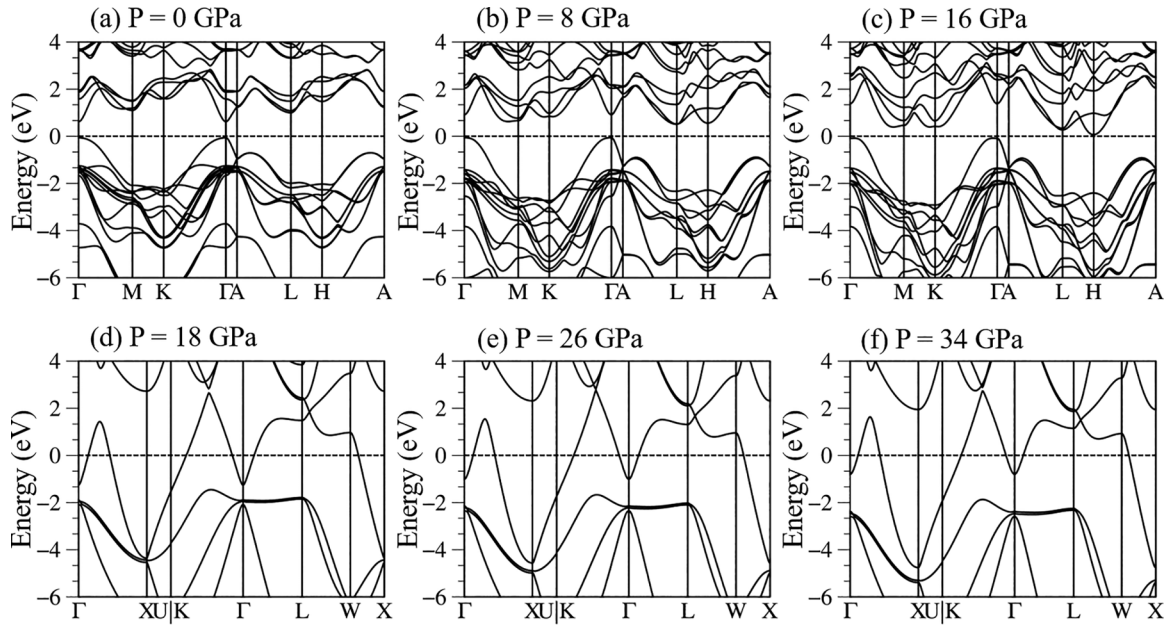

FIG. 4. The DFT electronic band structure of GaSe along the high-symmetry points under six presentative pressures: hexagonal GaSe at (a) 0 GPa, (b) 8 GPa, (c) 16 GPa, and rocksalt GaSe at (d) 18 GPa, (e) 26 GPa, and (f) 34 GPa. The highest occupied state is set at 0 eV as reference energy.

contrast, the low-frequency E^1_{1g} mode, which has a frequency determined by the interlayer force associated with a Se-Se bond and the intralayer bond-bending force (Fig. 3), showed an insensitivity characteristic to pressure. The little variation in frequency suggests that the large increase in the strength of the interlayer force is canceled out by the weakening intralayer Ga-Ga bond-bending force. Similar behavior was also found in the low-frequency Raman-active modes of multilayer InSe [59].

C. Electronic properties

The electronic properties of ε-GaSe crystals were investigated under varying pressure conditions using both DFT and GW levels of theory. Figures 4(a)–4(f) illustrate the electronic band structure of GaSe along the high-symmetry points of the first Brillouin zone (Fig. S3 [43]). In the absence of external pressure, the bulk GaSe exhibited a direct energy gap of 0.73 eV at the Γ point. The gap value is consistent with previous theoretical DFT work [19,36] but is rather smaller than that of the experimental observation [66,67] due to the absence of quasiparticle corrections. The electronic band gap of hexagonal GaSe is significantly enhanced ($E_g \sim 1.97$ eV) since the correction of electron-electron interactions (GW approximation) has been applied (the red curve in Figs. 5(a) and S7 [43]). This value is in good agreement with previous measurements [67,68].

To gain a deeper understanding of the modulation of the band structure under pressure, we performed calculations of the band-decomposed charge densities and orbital-projected electronic band structures. The obtained results, as illustrated in Figs. 5(c) and S8 [43], reveal that the valence band maxima (VBM)(Γ) is mainly composed of the out-of-plane bonding character of Ga-4p_z and Se-4p_z orbitals, while the conduction band minima (CBM)(Γ) is derived from the out-of-plane antibonding interactions of the Ga-4s and the Se-4p_z charge densities. The in-plane antibonding character of Ga-4s and Se-$(4p_x + 4p_y)$ orbitals are related to the CBM(L), the in-plane Ga-$(4p_x + 4p_y)$ and Se-$(4p_x + 4p_y)$ orbital characters being connected to the CBM(H). Therefore a large modification of the band states in the vicinity of the Γ point is attributed to changes in the coupling of layers, while interactions of in-plane orbitals of Ga and Se atoms will result in the changing of the band states at L and H.

Under pressurization, GaSe experiences notable modifications in its electronic band structure, attributed to increased dispersion in the conduction and valence energy subbands, which result from shortened interatomic distances. Consequently, the mobility of both electrons and holes is enhanced. The interaction between vertical orbitals is also enhanced due to the reduction of Se-Se interlayer and intralayer spacing, leading to a significant increase in the energy of the band-edge states at VBM(Γ) and CBM(Γ). This increase results in an enhanced direct band gap at the Γ point. Conversely, pressurization diminishes in-plane orbital interactions due to the gradual increase in the Ga-Se vertical distance, as illustrated in Fig. 1(f). As a result, the new CBM is shifted to the L point, causing a direct-to-indirect band-gap transition. These findings are consistent with previous theoretical predictions [69] and experimental measurements [36]. When the pressure is greater than 8.0 GPa, the CBM located at the H point becomes energetically more favorable compared to the CBM at the L point. This causes a crossover of the CBM from the L point to the H point [Fig. 4(c)]. At extremely high pressure, such as $P \sim 17$ GPa, GaSe undergoes a significant change in its electronic structure due to phase transition. Figure 4(d) displays the electronic band structure of the high-pressure rocksalt phase, revealing the absence of a band gap between occupied and unoccupied states, which indicates metallic behavior. This characteristic is further evidenced by the nature of electron localization functions.

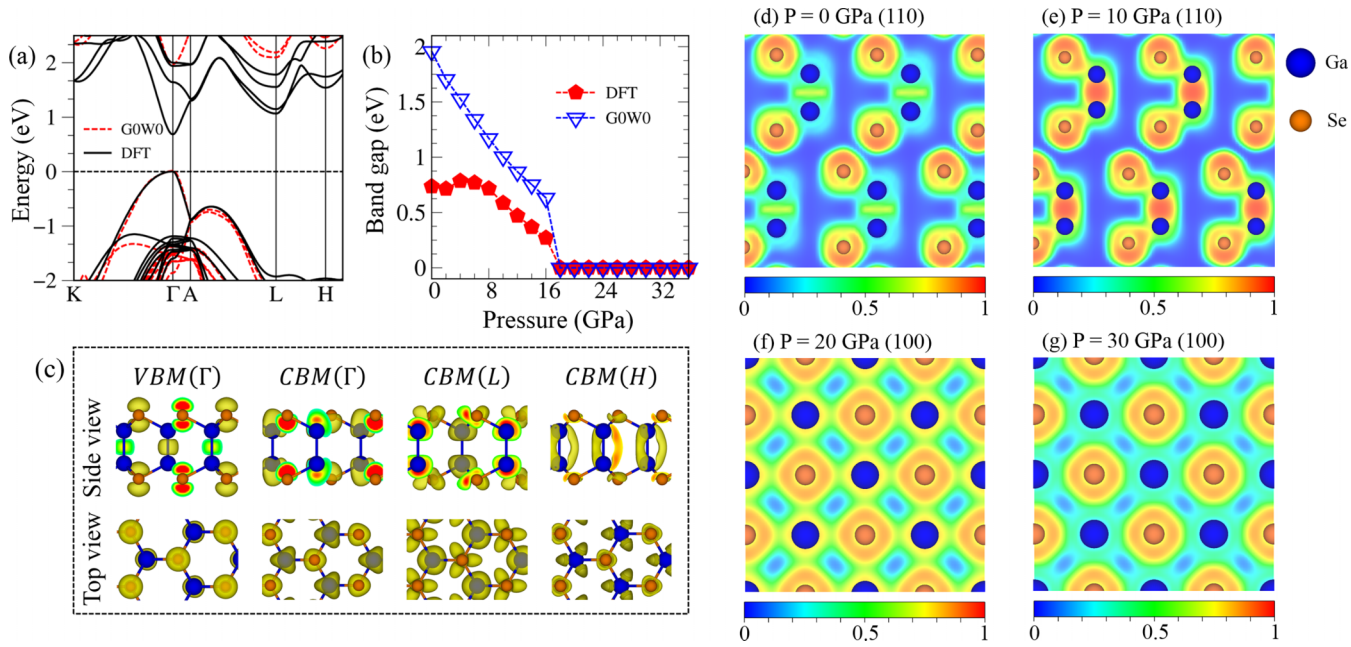

FIG. 5. (a) A comparison of the electronic band structure using GW and DFT approximations. The highest occupied state is set at 0 eV as reference energy. (b) Evolution of the band gap under DFT and GW approximations. (c) Top and side views of the band-decomposed charge densities at the critical band-edge states of the first layer of hexagonal GaSe. The electronic localization functions of GaSe at four representative pressures: hexagonal GaSe on the (110) plane at (d) 0 GPa, (e) 10 GPa, and rocksalt GaSe on the (100) plane at (f) 20 GPa and (g) 30 GPa.

Figure 5(b) illustrates the band-gap evolution of GaSe under varying pressures. It is important to highlight that the change in the band gap is a complex process. The band-gap adjustment, as predicted by the DFT level of theory, can be categorized into four distinct stages. In the first stage, the band gap (E_g) increases up to a maximum value of 0.8 eV at a pressure of 4 GPa, primarily due to a direct-to-indirect band-gap transition. Subsequently, as the applied strains increase, the electronic band gap gradually decreases due to the overlapping of wave functions, with a rate of change of approximately 0.1 eV/GPa. At a critical strain of $P =$ 17 GPa, the material undergoes a semiconductor-to-metal transition, as previously predicted. Beyond this pressure, the GaSe compound only exhibits metallic properties and the electronic band gap is completely absent. The band-gap evolution under GW approximation follows a different trend: the electronic band gap almost monotonically decreases as the external pressure increases, and the semiconductor–to-metal transition also occurs at 17 GPa. However, the direct-to-indirect band-gap transition cannot be detected on the pressure–band-gap diagram, since the energy difference between CBM(Γ) and CBM(L) at ambient conditions is relatively small to make an obvious signal under the GW corrections.

The electron localization function (ELF) can provide insight into orbital interactions and subsequent structural transformations [70,71]. Figures 5(d)–5(g) display the computed ELF, with renormalized scale values ranging from 0.0 to 1.0. These values correspond to the localization of electrons, ranging from very low density (the blue region) to highly localized density (the red region). At ambient conditions [Fig. 5(d)], a high charge density is observed between the Ga-Se and Ga-Ga bonds, indicating their covalent nature. Under external hydrostatic pressures below 17 GPa [Figs. 5(d)–5(e)], a noticeable change in the charge distribution between the two atoms is evident, especially in the vicinity of a Ga-Ga chemical bond. Despite the dramatic changing of the charge density, the interaction between two atoms remains covalent. Above 17 GPa [Fig. 5(f)], the charge density distribution around Ga and Se atoms undergoes a significant transformation due to a new atomic arrangement, and extra Ga-Se bonds are established. Beyond this critical pressure [Fig. 5(g)], the charge density distribution of Ga and Se atoms becomes more spherical and extended, with the average ELF reaching approximately 0.5, indicating homogeneous electron distribution and thus metallization.

D. Optical properties

Similar to other layered materials, GaSe exhibits strong anisotropic optical properties at ambient pressure [72], which is due to the significant difference in material environment along the x/y and z directions (Fig. S9). Figure 6(a) illustrates the imaginary part of dielectric functions $\varepsilon_2(\omega)$ of intrinsic GaSe for the light polarization along the z direction. Within the DFT-RPA (random phase approximation) framework, the absorption spectra indicate the presence of the optical gap/threshold frequency (E_g^o) at approximately 0.76 eV, and another prominent peak at about 1.2 eV. They are denoted by the red and blue triangles, respectively. These singularities arise from the vertical transition at the band-edge states vicinity of the Γ point, with their transition mechanism assigned in the inset of Fig. 6(a). The optical spectra display a significant blue shift due to the application of GW corrections,

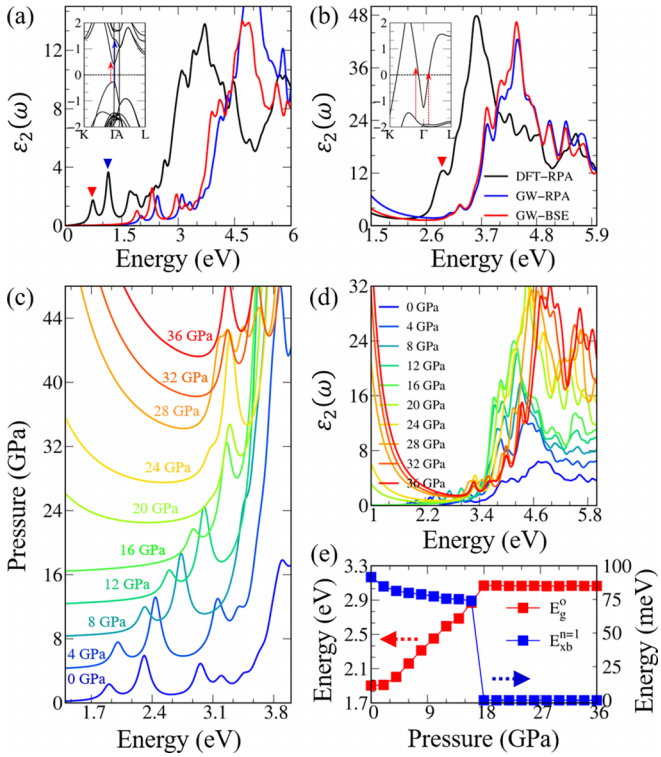

FIG. 6. The imaginary part of the dielectric function $\varepsilon_2(\omega)$ under different levels of theory of (a) hexagonal GaSe and (b) high-pressure rocksalt phase of GaSe. Inset: the transition mechanism of the first prominence interband transition. (c) The pressure-dependent optical excitation of GaSe, (d) similar plot as above but for a wider energy range (1 eV $\leqslant \omega \leqslant$ 6 eV), and (e) the evolution of the first interband transition and the exciton binding energy as functions of applied pressure.

while the opposite is true for the GW-BSE spectra as electron-hole interactions have been considered, e.g., $E_g^o \sim 1.9$ eV. Although the electron-hole interaction is weak compared to that of the single-layer system [23], the excitonic effects, evidenced by the difference in the GW-RPA and GW-BSE spectra, could be detected with the exciton binding energy $E_{xb} \simeq 90$ meV. The position of optical gap and the relatively weak exciton binding of GaSe in this work agree well with previous experimental measurements [58,67,68]. In Fig. 6(b) the optical absorbance spectra of rocksalt GaSe are presented. The absorbance spectra display a finite value at low frequency, indicating the dominance of the intraband transition of the free electrons around the Γ point. Additionally, there is a prominent interband transition at approximately 2.8 eV, with the excitation mechanism shown in the inset of Fig. 6(b). In this case the influence of electron-hole interactions on optical spectra is nearly undetectable due to the significant impact of electronic screening effects characterized by a high free electron density.

The low-frequency imaginary part of the dielectric function, $\varepsilon_2(\omega)$, is displayed in Fig. 6(c). The absorption curves exhibit no significant changes at low compression, but the optical spectra begin to shift towards higher frequencies at pressures exceeding 4 GPa, indicating an enhancement of the direct band gap at the Γ point. Beyond the critical pressure ($P = 17$ GPa), there is only little change in the low-frequency optical spectra. In addition to the tailoring of the optical gap, the external pressure is also induced to enhance the optical absorbance at the high-frequency region as indicated in Fig. 6(d). The changing of the optical gap and the exciton binding energy are analyzed in Fig. 6(e), where the modulation of the exciton binding energy (E_{xb}) is found to be a complex process. E_{xb} exhibits a remarkable change at low pressures ($P \leqslant 4$ GPa) due to the reduction/enhancement of the band-gap/electronic screening but then slowly decreases as higher external forces are applied. When the external pressure exceeds the critical phase-transition value, the electron-hole couplings drop dramatically to ∼0 eV, reflecting the metallic behavior of the rocksalt GaSe.

Figures 7(a)–7(c) show the energy-loss functions, defined as $Im[-1/\varepsilon(\omega)]$, which can provide valuable information about the charge screening ability and optical properties of materials. Previous studies [19] and Fig. 7(a) indicate that due to the weakly defined π and σ valence electrons in the sp^3 GaSe crystal, only one strong plasmon mode with energy greater than 8 eV exists, and the low-frequency collective excitation almost disappears. As shown in Fig. 7(d), $Im[-1/\varepsilon(\omega)]$ remains almost unchanged for pressures below 17 GPa, whereas the opposite is true for pressures beyond the critical value, such as $P = 20$ GPa. In this case, the free electron contribution is indicated by a strong peak emerging below 2.4 eV, consistent with the metallic behavior of rocksalt GaSe. The energy and intensity of the Drude contribution undergo significant changes with higher pressure application, as evidenced by the gradual shift of strong peaks towards higher energy, accompany with simultaneous broadening/suppression of intensity.

Figures 7(b) and 7(c) present the reflectance, $R(\omega)$, and absorbance spectra, $A(\omega)$, of GaSe. In the low-energy regime below 3.5 eV, the reflection is weakly energy dependent, with a typical value along the z direction of about 10% [Fig. 7(b)]. The absorption coefficient is almost negligible due to the absence of optical excitations [Fig. 7(c)]. In contrast, the reflectance and absorbance spectra exhibit significant fluctuations at energies greater than 4 eV, as expected for optically allowed transitions. The inverse value of the absorption coefficient mostly falls within a range of 200 Å, allowing for the easy absorption of photon beams penetrating the medium. This implies that GaSe has potential for optoelectronic applications. To fully comprehend the evolution of the optical properties of GaSe under pressurization, Figs. 7(e) and 7(f) show the changes in $R(\omega)$ and $A(\omega)$ under pressure. These spectra remain insensitive to external pressure below the critical value, $P \sim 17$ GPa; however, beyond this pressure the curves change dramatically. Most incident photons are reflected into the vacuum at the front surface, while a finite amount of light is absorbed even at low infrared frequencies, attributed to the free carrier concentration. The drastic decline in $R(\omega)$ and $A(\omega)$ indicates the plasmon modes discussed earlier. These behaviors have been verified by previous reflectance measurements [36]. Hydrostatic pressure has emerged as an effective tool for tailoring the electronic and optical properties of layered materials to meet specific application demands, such as electronic, optoelectronic, and photovoltaic devices.

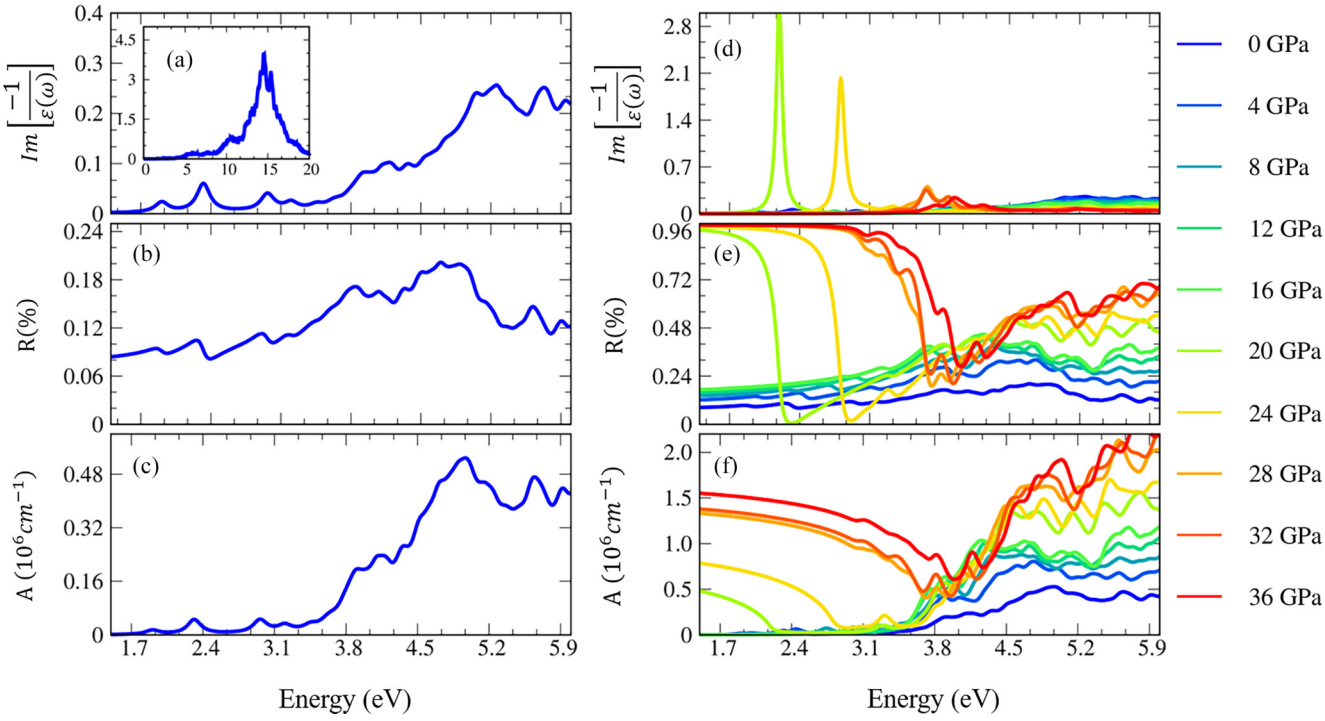

FIG. 7. (a) The energy-loss function, (b) absorbance, and (c) reflectance spectra of pristine ε − GaSe. (d)–(f) The change in optical properties under various pressures.

E. Phase-transition mechanism

The SS-NEB computational method, widely used in the field of materials science, was employed for a comprehensive investigation of the structural phase transformation in GaSe. The calculation involved 29 intermediate images, with a root-mean-square force convergence of 0.03 eV/Å. The mechanism governing the hexagonal-to-rocksalt phase transition can be described as a two-stage process: (1) hexagonal → tetragonal and (2) tetragonal → rocksalt, as illustrated in Fig. 8(a).

In Fig. 8(b) the pressure-dependent potential energy curves are presented, depicting the energy of each image at the corresponding pressures. These curves reveal two distinct peaks, occurring at image 9 and image 24, which correspond to the breaking and formation of Ga-Ga and Ga-Se chemical bonds, respectively. With increasing pressure, the rocksalt phase demonstrates enhanced stability, consistent with the observed behavior of GaSe under high-pressure conditions. Notably, at image 16, a metastable structure emerges when the external pressure surpasses 12 GPa. The minimum energy required for the hexagonal-to-rocksalt transition at 17 GPa is approximately 210 meV per atom, highlighting the considerable energy demand for breaking the robust Ga-Ga covalent bonds.

Figure 8(c) provides valuable insights into the structural phase transition by illustrating internal structural parameters, specifically, the α angle and the c/a ratio. Additionally, Fig. 8(d) depicts the energy profiles at specific image numbers corresponding to the transition pressure. During the initial transition stage, a notable increase in the hexagonal angle (α), along with a gradual decrease in the axial c/a ratio, is observed. At image 9, the Ga-Ga covalent bonds become unstable under the applied compressive forces, leading to their breakage. Subsequently, by image 16, both the c/a ratio and the α angle reach values of 2.7 and 90 degrees, respectively, indicating the emergence of a tetragonal metastable phase. In the second stage we observe minimal changes in the α angle and c/a ratio. During this stage, adjacent half-rigid layers alternately slide along the basal plane, resulting in the contact between Ga and Se atoms from these layers. This interaction leads to the formation of metallic bonds at image 24, eventually resulting in the creation of a perfect octahedral structure in the rocksalt GaSe through rearrangement and bonding by image 30. These observations provide compelling evidence for the complete transformation of the hexagonal phase into the rocksalt phase.

IV. CONCLUSIONS

In conclusion, this study provides a comprehensive investigation of the phase transition, atomic vibration, electronic and optical properties, and excitonic effects of ε-GaSe under external pressure up to 40 GPa. The first-principles calculations show that ε-GaSe undergoes a structural phase transition from the hexagonal phase to the rocksalt phase at around 17 GPa, consistent with previous experimental and theoretical studies. The study reveals that the electronic properties of ε-GaSe undergo a semiconductor-to-metal transition at the transition point, with a sharp drop in the band gap due to the shift of the valence-band maximum at the Γ point and the conduction-band minimum at the L and H point in the Brillouin zone.

Additionally, the study analyzed the phonon vibrations of ε-GaSe and found that the phonon frequencies increase gradually with increasing pressure up to the transition point,

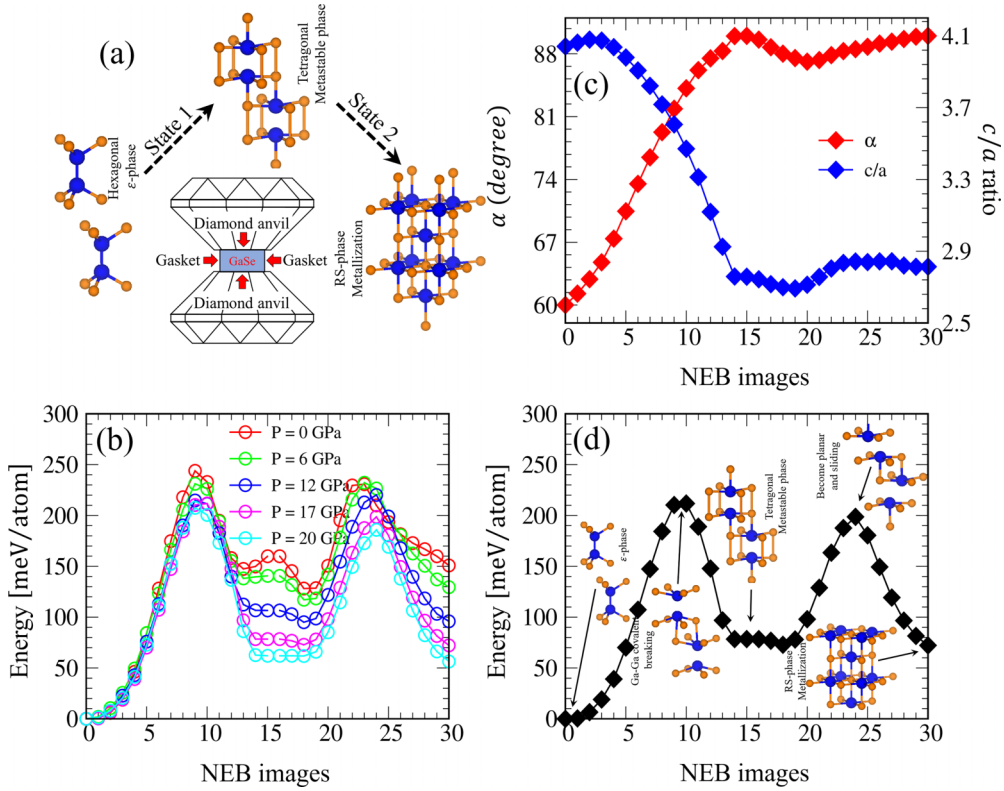

FIG. 8. (a) The proposed phase-transition mechanism from the hexagonal phase of ε-GaSe to the rocksalt phase. The transition can be considered a two-step process: The first transition state corresponds to the transformation from the hexagonal phase to a tetragonal intermediate phase. The second transition state involves the transformation from the tetragonal intermediate phase to the rocksalt phase. (b) Pressure-dependent potential curves showing the variation in the energy barrier as a function of pressure. (c) Internal structural parameters dependent on NEB images (α angle and c/a ratio). (d) The potential curve for the transition from the hexagonal phase of GaSe to the rocksalt phase at the equilibrium pressure of $P = 17$ GPa. Each potential curve in (b) and (d) corresponds to its respective pressure level, progressing from one end to the other.

mostly due to the increased interlayer interactions and reduced intralayer bondings. The optical properties of ε-GaSe were also analyzed, revealing that the optical gap increases gradually with increasing pressure up to the transition point, and then drops sharply at the transition, in agreement with the electronic band gap. Moreover, the excitonic effects, such as the exciton binding energy and the oscillator strength, were found to be highly sensitive to pressure, with a significant drop to 0 eV observed at the transition pressure.

Finally, the SS-NEB method was used to analyze the phase-transition mechanism of ε-GaSe, which showed that the transition involves a two-step process with an intermediate state before the final transformation to the rocksalt phase. The activation energy for the transformation was estimated to be around 210 meV. The results obtained from this study provide insights into the phase-transition mechanism of ε-GaSe and can be useful in designing new materials for electronic and optoelectronic applications. Further experimental studies could validate these findings and pave the way for practical applications.

ACKNOWLEDGMENT

This work was supported by the Vietnam Ministry of Education and Training under Grant No. B2023-TCT-03.

There are no conflicts of interest to declare.

[1] Z. Ben Aziza, H. Henck, D. Pierucci, M. G. Silly, E. Lhuillier, G. Patriarche, F. Sirotti, M. Eddrief, and A. Ouerghi, ACS Nano **10**, 9679 (2016).

[2] Z. Zhu, Y. Cheng, and U. Schwingenschlögl, Phys. Rev. Lett. **108**, 266805 (2012).

[3] H. Nitta, T. Yonezawa, A. Fleurence, Y. Yamada-Takamura, and T. Ozaki, Phys. Rev. B **102**, 235407 (2020).

[4] X. Zhou, J. Cheng, Y. Zhou, T. Cao, H. Hong, Z. Liao, S. Wu, H. Peng, K. Liu, and D. Yu, J. Am. Chem. Soc. **137**, 7994 (2015).

[5] L. Karvonen, A. Säynätjoki, S. Mehravar, R. D. Rodriguez, S. Hartmann, D. R. T. Zahn, S. Honkanen, R. A. Norwood, N. Peyghambarian, K. Kieu *et al.*, Sci. Rep. **5**, 10334 (2015).

[6] P. Hu, L. Wang, M. Yoon, J. Zhang, W. Feng, X. Wang, Z. Wen, J. C. Idrobo, Y. Miyamoto, D. B. Geohegan *et al.*, Nano Lett. **13**, 1649 (2013).

[7] Y. Lu, J. Chen, T. Chen, Y. Shu, R.-J. Chang, Y. Sheng, V. Shautsova, N. Mkhize, P. Holdway, H. Bhaskaran *et al.*, Adv. Mater. **32**, 1906958 (2020).

[8] P. Hu, Z. Wen, L. Wang, P. Tan, and K. Xiao, ACS Nano **6**, 5988 (2012).

[9] X. Li, M.-W. Lin, J. Lin, B. Huang, A. A. Puretzky, C. Ma, K. Wang, W. Zhou, S. T. Pantelides, M. Chi *et al.*, Sci. Adv. **2**, e1501882 (2016).

[10] Z. Chen, S. Chu, J. Chen, H. Chen, J. Zhang, X. Ma, Q. Li, and X. Chen, Nano Energy **56**, 294 (2019).

[11] H. L. Zhuang and R. G. Hennig, Chem. Mater. **25**, 3232 (2013).

[12] Y. Fan, X. Ma, X. Liu, J. Wang, H. Ai, and M. Zhao, J. Phys. Chem. C **122**, 27803 (2018).

[13] T. Wieting and J. Verble, Phys. Rev. B **5**, 1473 (1972).

[14] R. Longuinhos and J. Ribeiro-Soares, Phys. Chem. Chem. Phys. **18**, 25401 (2016).

[15] S. Y. Lim, J.-U. Lee, J. H. Kim, L. Liang, X. Kong, T. T. H. Nguyen, Z. Lee, S. Cho, and H. Cheong, Nanoscale **12**, 8563 (2020).

[16] D. J. Late, B. Liu, H. R. Matte, C. Rao, and V. P. Dravid, Adv. Funct. Mater. **22**, 1894 (2012).

[17] D. J. Late, B. Liu, J. Luo, A. Yan, H. R. Matte, M. Grayson, C. Rao, and V. P. Dravid, Adv. Mater. **24**, 3549 (2012).

[18] X. Li, L. Basile, B. Huang, C. Ma, J. Lee, I. V. Vlassiouk, A. A. Puretzky, M.-W. Lin, M. Yoon, and M. Chi, ACS Nano **9**, 8078 (2015).

[19] Y. Ma, Y. Dai, M. Guo, L. Yu, and B. Huang, Phys. Chem. Chem. Phys. **15**, 7098 (2013).

[20] M. Rahaman, M. Bejani, G. Salvan, S. A. Lopez-Rivera, O. Pulci, F. Bechstedt, and D. R. Zahn, Semicond. Sci. Technol. **33**, 125008 (2018).

[21] A. Kumar and P. K. Ahluwalia, Eur. Phys. J. B **85**, 186 (2012).

[22] H. Huang, P. Wang, Y. Gao, X. Wang, T. Lin, J. Wang, L. Liao, J. Sun, X. Meng, Z. Huang *et al.*, Appl. Phys. Lett. **107**, 143112 (2015).

[23] G. Antonius, D. Y. Qiu, and S. G. Louie, Nano Lett. **18**, 1925 (2018).

[24] V. K. Dien, N. T. Han, W. Bang-Li, K.-I. Lin, and M.-F. Lin, Adv. Theory Simul. **6**, 2200950 (2023).

[25] A. Mujica, A. Rubio, A. Munoz, and R. Needs, Rev. Mod. Phys. **75**, 863 (2003).

[26] H. Xia, Q. Xia, and A. L. Ruoff, Phys. Rev. B **47**, 12925 (1993).

[27] S. Limpijumnong and W. R. L. Lambrecht, Phys. Rev. B **63**, 104103 (2001).

[28] S. Limpijumnong and W. R. L. Lambrecht, Phys. Rev. Lett. **86**, 91 (2001).

[29] S. Uehara, T. Masamoto, A. Onodera, M. Ueno, O. Shimomura, and K. Takemura, J. Phys. Chem. Solids **58**, 2093 (1997).

[30] B. C. da Silva, J. Couto, O. D. Damasceno, H. Obata, C. A. Senna, B. S. Archanjo, F. Iikawa, and M. A. Cotta, ACS Omega **7**, 44199 (2022).

[31] N. E. Christensen and I. Gorczyca, Phys. Rev. B **50**, 4397 (1994).

[32] C. B. Maliakkal, M. Gokhale, J. Parmar, R. D. Bapat, B. A. Chalke, S. Ghosh, and A. Bhattacharya, Nanotechnology **30**, 254002 (2019).

[33] S. Assali, J. Greil, I. Zardo, A. Belabbes, M. De Moor, S. Koelling, P. M. Koenraad, F. Bechstedt, E. P. A. Bakkers, and J. E. Haverkort, J. Appl. Phys. **120**, 044304 (2016).

[34] L. Ghalouci, B. Benbahi, S. Hiadsi, B. Abidri, G. Vergoten, and F. Ghalouci, Comput. Mater. Sci. **67**, 73 (2013).

[35] K. Dunn and F. Bundy, Appl. Phys. Lett. **36**, 709 (1980).

[36] U. Schwarz, D. Olguin, A. Cantarero, M. Hanfland, and K. Syassen, Phys. Status Solidi B **244**, 244 (2007).

[37] N. Q. Diep, S. K. Wu, C. W. Liu, S. H. Huynh, W. C. Chou, C. M. Lin, D. Z. Zhang, and C. H. Ho, Sci. Rep. **11**, 19887 (2021).

[38] A. Kulibekov, H. Olijnyk, A. Jephcoat, Z. Salaeva, S. Onari, and K. Allakhverdiev, Phys. Status Solidi B **235**, 517 (2003).

[39] M. Gauthier, A. Polian, J. M. Besson, and A. Chevy, Phys. Rev. B **40**, 3837 (1989).

[40] J. Besson, K. Jain, and A. Kuhn, Phys. Rev. Lett. **32**, 936 (1974).

[41] S. Grimme, J. Antony, S. Ehrlich, and H. Krieg, J. Chem. Phys. **132**, 154104 (2010).

[42] A. Togo, J. Phys. Soc. Jpn. **92**, 012001 (2023).

[43] See Supplemental Material at http://link.aps.org/supplemental/10.1103/PhysRevB.108.205150 for in-depth information on the following: possible phases of GaSe under ambient pressure; cohesive energy as a function of volume for the hexagonal phase under different exchange-correlation functions; first Brillouin zone of hexagonal and rocksalt GeSe; phonon properties of hexagonal and rocksalt GaSe, both with and without the influence of Born effective charges and dielectric constants; phonon density of states of GaSe as a function of hydrostatic pressure, specific heat capacity, GW-band structure, and orbital-projected electronic band structure; polarization of the optical properties of GaSe; and GW-BSE test for Cu using various levels of theory. It also contains Ref. [73].

[44] G. Samsonidze, M. Jain, J. Deslippe, M. L. Cohen, and S. G. Louie, Phys. Rev. Lett. **107**, 186404 (2011).

[45] A. A. Mostofi, J. R. Yates, Y.-S. Lee, I. Souza, D. Vanderbilt, and N. Marzari, Comput. Phys. Commun. **178**, 685 (2008).

[46] R. Cutkosky, Phys. Rev. **96**, 1135 (1954).

[47] S. Hirata and M. Head-Gordon, Chem. Phys. Lett. **314**, 291 (1999).

[48] J. Deslippe, C. D. Spataru, D. Prendergast, and S. G. Louie, Nano Lett. **7**, 1626 (2007).

[49] L. Yang, Nano Lett. **11**, 3844 (2011).

[50] Z. Zhu, J. Guan, and D. Tománek, Phys. Rev. B **91**, 161404(R) (2015).

[51] A. Kuhn, A. Chevy, and R. Chevalier, Phys. Status Solidi A **31**, 469 (1975).

[52] D. V. Rybkovskiy, N. R. Arutyunyan, A. S. Orekhov, I. A. Gromchenko, I. V. Vorobiev, A. V. Osadchy, E. Y. Salaev, T. K. Baykara, K. R. Allakhverdiev, and E. D. Obraztsova, Phys. Rev. B **84**, 085314 (2011).

[53] V. M. Kaminskii, Z. D. Kovalyuk, M. N. Pyrlya, S. V. Gavrilyuk, and V. V. Netyaga, Inorg. Mater. **41**, 793 (2005).

[54] S. Nagel, A. Baldereschi, and K. Maschke, J. Phys. C **12**, 1625 (1979).

[55] S. Y. Sarkisov, A. V. Kosobutsky, and S. D. Shandakov, J. Solid State Chem. **232**, 67 (2015).

[56] M. Abdullah, G. Bhagavannarayana, and M. Wahab, J. Cryst. Growth **312**, 1534 (2010).

[57] J. Terhell and R. Lieth, Phys. Status Solidi A **5**, 719 (1971).

[58] C.-W. Liu, J.-J. Dai, S.-K. Wu, N.-Q. Diep, S.-H. Huynh, T.-T. Mai, H.-C. Wen, C.-T. Yuan, W.-C. Chou, and J.-L. Shen, Sci. Rep. **10**, 1 (2020).

[59] G. Huang, Y. Zhou, Z.-Y. Dong, W.-J. Li, K.-J. Bu, S. Zhou, T. Wang, X.-J. Lü, and X.-J. Chen, J. Phys. Chem. C **126**, 6344 (2022).

[60] S. S. Parashari, S. Kumar, and S. Auluck, Phys. B: Condens. Matter **403**, 3077 (2008).
[61] E. Pop, V. Varshney, and A. K. Roy, MRS Bull. **37**, 1273 (2012).
[62] A. Molina-Sánchez and L. Wirtz, Phys. Rev. B **84**, 155413 (2011).
[63] C. Kittel and P. McEuen, *Introduction to Solid State Physics* (John Wiley & Sons, New York, 2018).
[64] Y. Jiang, S. Cai, Y. Tao, Z. Wei, K. Bi, and Y. Chen, Comput. Mater. Sci. **138**, 419 (2017).
[65] K. Jeong, S. Park, D. Park, M. Ahn, J. Han, W. Yang, H.-S. Jeong, and M.-H. Cho, Sci. Rep. **7**, 1 (2017).
[66] E. Aulich, J. Brebner, and E. Mooser, Phys. Status Solidi B **31**, 129 (1969).
[67] J. Camassel, P. Merle, H. Mathieu, and A. Gouskov, Phys. Rev. B **19**, 1060 (1979).
[68] R. Le Toullec, N. Piccioli, and J. C. Chervin, Phys. Rev. B **22**, 6162 (1980).
[69] V. Brudnyi, A. Kosobutsky, and S. Y. Sarkisov, Semiconductors **44**, 1158 (2010).
[70] H. Zheng, X.-B. Li, N.-K. Chen, S.-Y. Xie, W. Q. Tian, Y. Chen, H. Xia, S. B. Zhang, and H.-B. Sun, Phys. Rev. B **92**, 115307 (2015).
[71] Y. Wang, F. Tian, D. Li, D. Duan, H. Xie, B. Liu, Q. Zhou, and T. Cui, Chin. Phys. B **28**, 056104 (2019).
[72] A. Seyhan, O. Karabulut, B. Akį noğlu, B. Aslan, and R. Turan, Cryst. Res. Technol. **40**, 893 (2005).
[73] P. Johnson and R. Christy, Phys. Rev. B **11**, 1315 (1975).

Correction: A typographical error in the postal code for the third and fourth affiliations has been fixed.